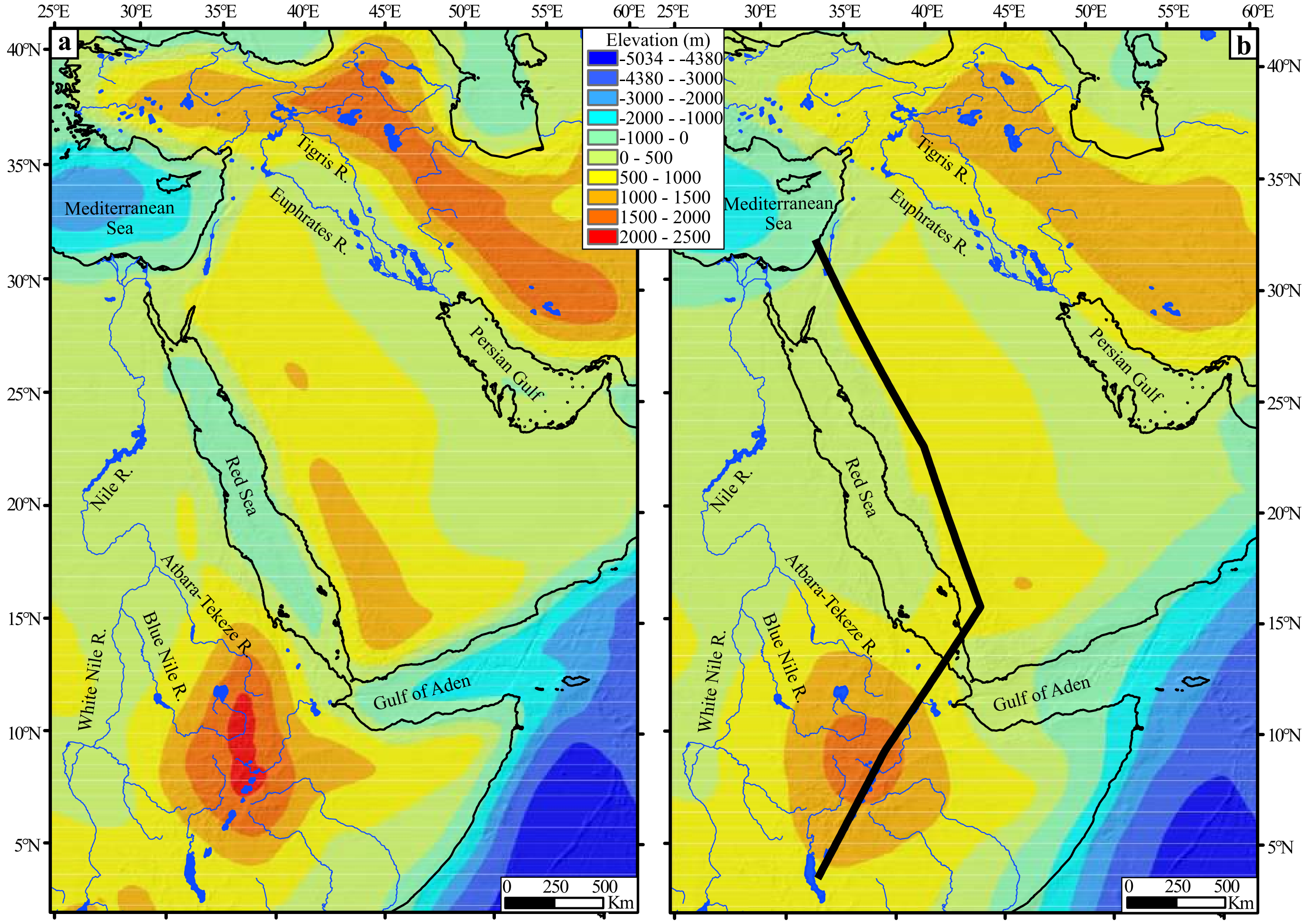

Fig. 7. Filtered topographies at 200 (a) and 400 km (b). The solid black line in (b) indicates the trace of the profiles represented in Fig. 13.

1996), to evaluate the relationship among erosion, precipitation and tectonic uplift (Thiede et al., 2004; Bookhagen et al., 2005; Hoke et al., 2005; Champagnac et al., 2009), to study the impact of rock erodibility on mountainous relief (Kühni and Pfiffner, 2001), and to catch drainage reorganization or fluvial terrace location (Godard et al., 2010; Stüwe et al., 2009; Wegmann and Pazzaglia, 2009). The difference between maximum and minimum topography at each point of the profile quantifies the local relief that, in a non-glaciated area, is a good approximation of fluvial incision (Isacks, 1992; Telbisz et al., 2013; see Fig. S2). Molin et al. (2004) showed that, in active tectonic landscapes, regions of high local relief often correspond with areas of incision in response to uplift.

To investigate the geometry of the EAAS, eight swath profiles have been extracted from the ETOPO2022 DEM by tracing 25 equally spaced topographic profiles into a 100 km wide observation window (Fig. 8). The elevation data along each profile have been sampled every 2 km. According to the configuration of the filtered topography at 200 and 400 km (Figs. 7a, b) we traced six profiles roughly orthogonal to the Red Sea (SW-NE trend), one orthogonal to the Main Ethiopian Rift and one along the crest of the swell, from Ethiopia to the border between Syria and Turkey. The first seven profiles clearly show a ridge-like topography interrupted by the Red Sea or the MER with a geometry varying from north to south (Fig. 8):

Profile 1. The ridge is ~800 km wide from Israel to the Euphrates-Tigris plain with a maximum elevation of ~800 m in coincidence with the Israel-Jordan Plateau. The higher peaks on the plateau correspond to the Harrat Ash Shaam volcanic province where volcanic edifices are 1600 m high.

Profile 2. The ridge considerably enlarges up to ~1000 km with a maximum elevation of ~1000 m occurring entirely on the Arabian margin of the Red Sea. As for Profile 1, the elevation gradually and smoothly decreases down to zero toward NE.

Profile 3. The ridge mostly extends in the Arabian margin with an amplitude of ~1100 km and an elevation of ~1000 m. In the Egypt margin, a small plateau (~200 km in width) at ~600 m of elevation may represent the northwestern portion of the ridge. The highest portion (~1000 m) is characterized by the edifices of three volcanic provinces named Harrat Qalib, Harrat Kura, Harrat Hutaymah arriving at ~2000 m of elevation (Coleman et al., 1983).

Profile 4. A pronounced ridge ~1200 km wide and ~1000 m high. ~200 km of the total width is observable in the Sudan margin while the remaining characterizes the Arabian one. The area with the maximum elevation is centered in the Arabian Plateau. Here the volcanoes of the Harrat Rahat and Harrat Al Kishb volcanic provinces tower up to an elevation of ~1500 m (Coleman et al., 1983).

Profiles 5 and 6. To the southernmost portion of the study area (Profiles 5 and 6) the ridge is first centered in the Red Sea (Profile 5) and then mostly in the southwestern margin (Profile 6) with a maximum width of ~1600 km and an elevation reaching ~2500 m in coincidence with the Ethiopian-Somalian and Yemen plateaux.

Profile 7. Orthogonal to the Main Ethiopian Rift and shows the southernmost portion of the swell. In particular, the bulge presents the highest elevation (~2700 m) and extends for >1300 km from the Sudan and Somalia lowlands, in accordance with previous studies (Sembroni et al., 2016b, 2021). The peaks seen in the maximum topography correspond with the major volcanoes that lie on the Ethiopian-Somalian

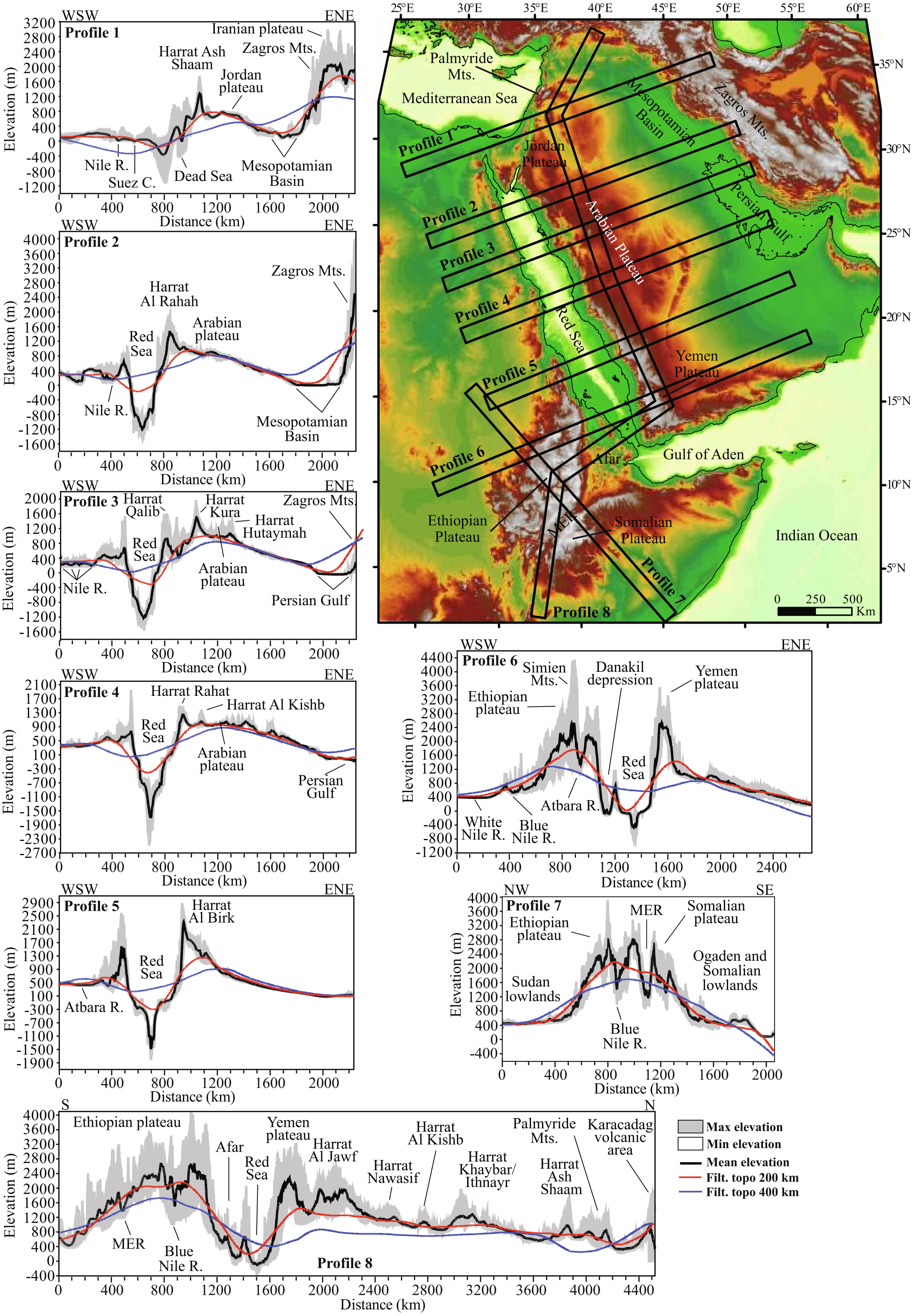

Fig. 8. Swath profiles extracted across the study area. To compare the general topographic configuration with the filtered topography, two curves extracted from the topography filtered at 200 and 400 km (Figs. 7a, b) along the middle line of each swath have been included in the plots. The trace of each swath is represented in the upper right map.

plateau.

Profile 8. Across the crest of the topography anomaly highlighted in the filtered topographies at 200 and 400 km (Figs. 7a, b). The EAAS extends for a total length of ~4000 km from Ethiopia to Jordan with a mean elevation gradually decreasing from ~2700 m (Ethiopia) to ~600 m (Jordan). The surface of the swell is characterized by the high-standing Ethiopian-Somalian and Yemen plateaux and by several volcanic provinces (harrats) in the Arabian portion which make its top surface irregular.

In all profiles, the local relief is low (< 200 m) on the ridge top and flanks, especially in the Arabian one, whereas is moderate to high (400–1000 m) in coincidence with the Red Sea and the MER and Afar margins (Fig. S2).

To better describe the topographic configuration of the swell, two curves extracted from the topography filtered at 200 and 400 km along the middle line of each swath have been included in the swath profiles (Fig. 8). The first curve (200 km in wavelength) roughly approximates the mean topography except for the Red Sea area where shorter wavelengths of topography are dominant. The second curve (400 km in wavelength) appears coincident with the mean topography of the Arabian (eastern) portion of the swell while deviates from the general pattern in the western part. It has negative values at the Indian Ocean coast.

In summary, the analysis of topography by swath profiles allows us to quantitatively define the geometry of the EAAS. It is confined between the Egypt-Sudan lowlands to the SW and the Euphrates-Tigris plain to the NE and characterized by an amplitude and an elevation gradually increasing from north (800 km and 800 m) to south (1600 km and 2700 m). The same trend is present in the topography at the Red Sea margins where the northern portion shows peaks approaching ~1000 m (southwestern margin) and ~2000 m (northeastern margin) of elevation which gradually increase at ~2500 m and ~2900 m respectively to the south. According to several studies (see Stüwe et al., 2022 and references therein) these high elevated portions along the margins of the Red Sea have been caused by the flexural uplift of the rift shoulders whose effect over time has been amplified by complex feedback between seafloor spreading and erosion. The same process has been studied by Weissel et al. (1995) and Sembroni et al. (2016a, 2016b) along the Afar escarpment and the Main Ethiopia Rift margins. The authors found increasing values of flexural uplift from ~500 m in the north to ~1200 m in the south.

5.3. *The flexural uplift on the margins of the Red Sea*

Although the EAAS represents a long wavelength signal, the opening of the Red Sea rift, with its maximum extent of ~300 km, may have modulated the expression of the swell partially hiding its topographic signal. To quantify such a topographic component, the uplift of rift flanks has been modeled as a flexural response to the unloading of the lithosphere due to extension.

Flexural deflections of the Earth lithosphere can support loads elastically on short wavelengths rather than having an isostatic floating equilibrium, which we expect to hold on long wavelengths, all relative to the effective elastic thickness. Elastic flexure with infill is governed by the equation (Turcotte and Schubert, 1982):

$$\nabla^2\left[D(x,y)\nabla^2 w(x,y)\right] + \Delta\rho g w = q(x,y) \tag{1}$$

where *w(x,y)* is the deflection of the surface, *D(x, y)* the flexural rigidity, Δρ the density contrast between the crust and the mantle, *g* the acceleration due to gravity, and *q(x, y)* the vertical load applied or removed from the lithosphere. The solution of eq. (1) for the case of a broken lithosphere is (Turcotte and Schubert, 1982):

$$w(x) = w_0 e^{-x/\alpha} \cos\frac{x}{\alpha} \tag{2}$$

$$D = \frac{E T_e^3}{12(1-\nu^2)} \tag{3}$$

$$\alpha = \left(\frac{4D}{g(\rho_m - \rho_a)}\right)^{1/4} \tag{4}$$

where w_0 is the maximum vertical displacement caused by the load, α the flexural wavelength, T_e is the equivalent elastic thickness of the lithosphere, ρ_m mantle, and ρ_a air density.

In this study, nine topographic profiles (see Figs. S3, S4), extracted from a smoothed topography (30 km radius smoothing circular window – to remove peaks related to the biggest volcanic edifices), have been fitted by eq. (2) using an iterative, nonlinear least-squares fitting algorithm (as implemented in MatLab). Confidence bounds for fitted coefficients and prediction bounds for the fitting curve reflect a 95% confidence interval (see Fig. S4). Lastly, the data extracted along each profile have been interpolated by a triangulation algorithm in ArcGIS environment obtaining a TIN surface (Fig. 9a).

The results indicate a progressive increase in flexural uplift from north to south on both the Red Sea margins, except for the northernmost portion of the African margin (Fig. 9a). This is in accordance with thermochronological data which dated the beginning of rifting at 26–20 Ma in the southern portion of the Red Sea (Boone et al., 2021 and references therein). On average, the western margin is characterized by lower values (415–3382 m) than the eastern one (1447–2771 m). The deformation related to flexural (flexural wavelength) is consistent up to a maximum of ~250 km from the Red Sea margins (Fig. 9a; Table S1). The inferred elastic thickness varies from 13 to 76 km on the African side (37.7 km average) and from 20 to 29 in the Arabian one (25.2 km on average; Table S1) in agreement with previous studies (Chen et al., 2015; Sreenidhi et al., 2023). In particular, Chen et al. (2015) correlate the relatively small T_e values and the low S-wave velocity anomaly with the elevated topography of the region concluding that the uplift is supported by hot mantle.

To distinguish the different components of topography across the Red Sea area, a topographic profile has been extracted along the southern portion of the Red Sea where the flexural uplift is higher (Fig. 9a). Together with it we plotted the flexural uplift extracted from Fig. 9a and the two curves from the filtered topographies (Figs. 7a, b). The graph shows that the present topography is dominated by the flexural component only in the first ~200 km from the rift shoulders. Beyond that distance, the topography is better approximated by the filtered topography at 400 km (Fig. 9b), consistent with the expectation of dynamic or isostatic control of topography at long wavelengths.

5.4. *Residual, dynamic topography, and river networks*

Filtered analysis of actual topography can be complemented by considering anomalous topography relative to what is expected isostatically from a given lithospheric model, i.e. residual topography (e.g., Panasyuk and Hager, 2000). Our approach for estimating residual topography follows the approach of Becker et al. (2014) and Faccenna and Becker (2020). As in Faccenna and Becker (2020), we use a modification of the CRUST1 (Laske et al., 2013) global crustal thickness model which we continuously update, e.g. earlier by merging data from the compilation of Gvirtzman et al. (2016) and other studies. Compared to Faccenna and Becker (2020), we here also include a few newer studies as compiled by Boyce et al. (2023) for an updated Moho map that is shown in Fig. 10a (see Boyce et al., 2023, for references). A smoothed version of that new crustal thickness model is then used along with CRUST1 density anomalies to estimate residual, i.e. non-isostatic, topography, ignoring any lateral lithospheric mantle density or thickness variations, for simplicity.

The resulting, updated residual topography map (Fig. 10b) is overall very similar to that of Faccenna and Becker (2020) and Stephenson et al.

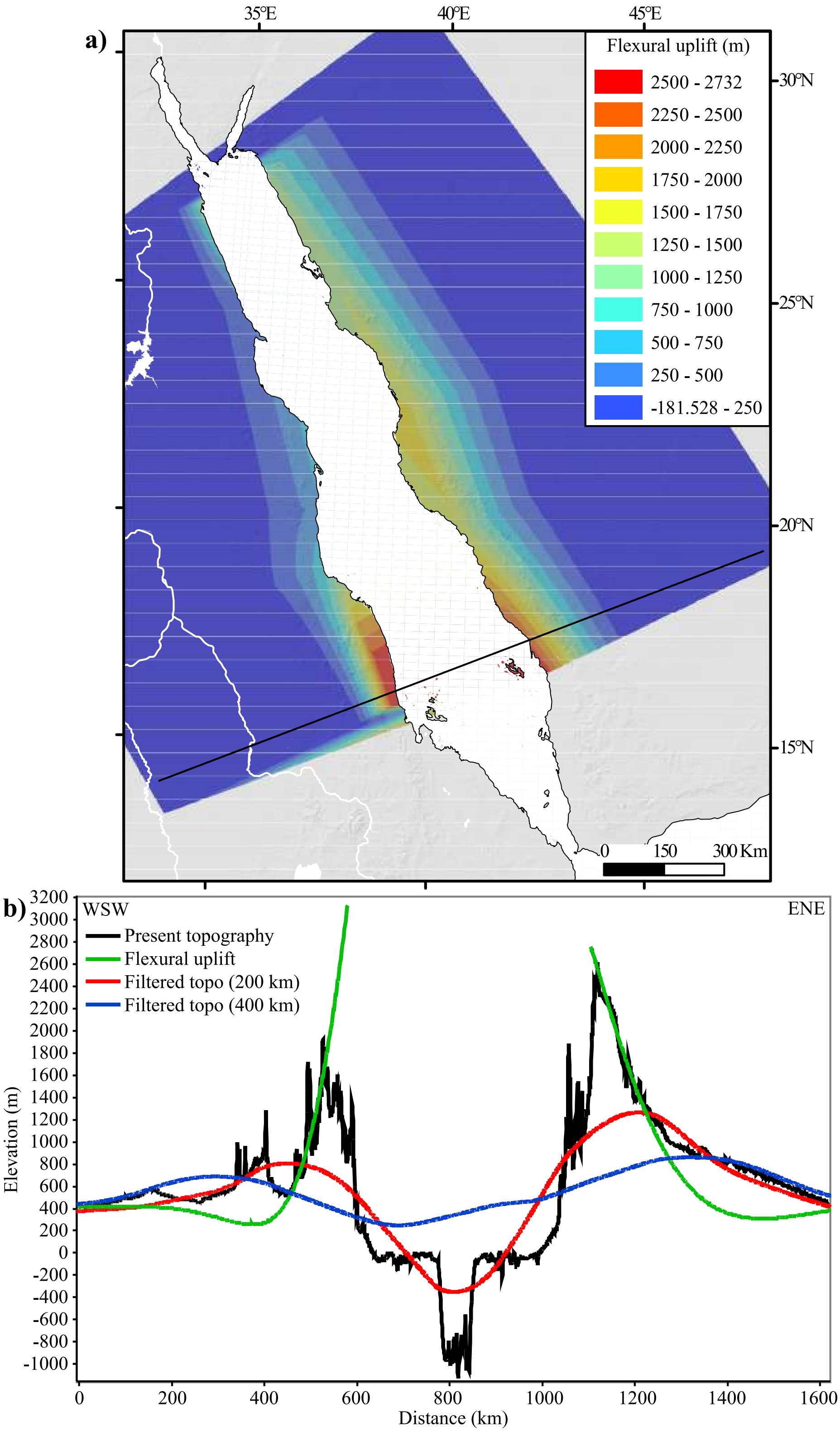

Fig. 9. a) Map of the flexural uplift calculated along the Red Sea region; the solid black line represents the trace of the profile shown in Fig. 9b; b) topographic profile extracted from the ETOPO2022 global elevation model. Along the same trace the flexural uplift and the filtered topographies at 200 and 400 km (Figs. 7a, b) have been extracted for comparison. (For interpretation of the references to colour in this figure legend, the reader is referred to the web version of this article.)

(2024); it shows positive anomalies (0–2000 m) concentrated in eastern Africa and along the Red Sea and the western portion of the Arabia Peninsula. The highest values (>2000 m) characterize the Main Ethiopian Rift, the southwestern portion of the Arabian Peninsula, and the Red Sea. Values between 0 and 2000 m are found to the west of the Nile River, in the central portion of the Arabian Peninsula, and in the western and central sectors of Anatolia. Negative values appear along the Mesopotamian Basin and the Persian Gulf area (−3000–0 m), in coincidence

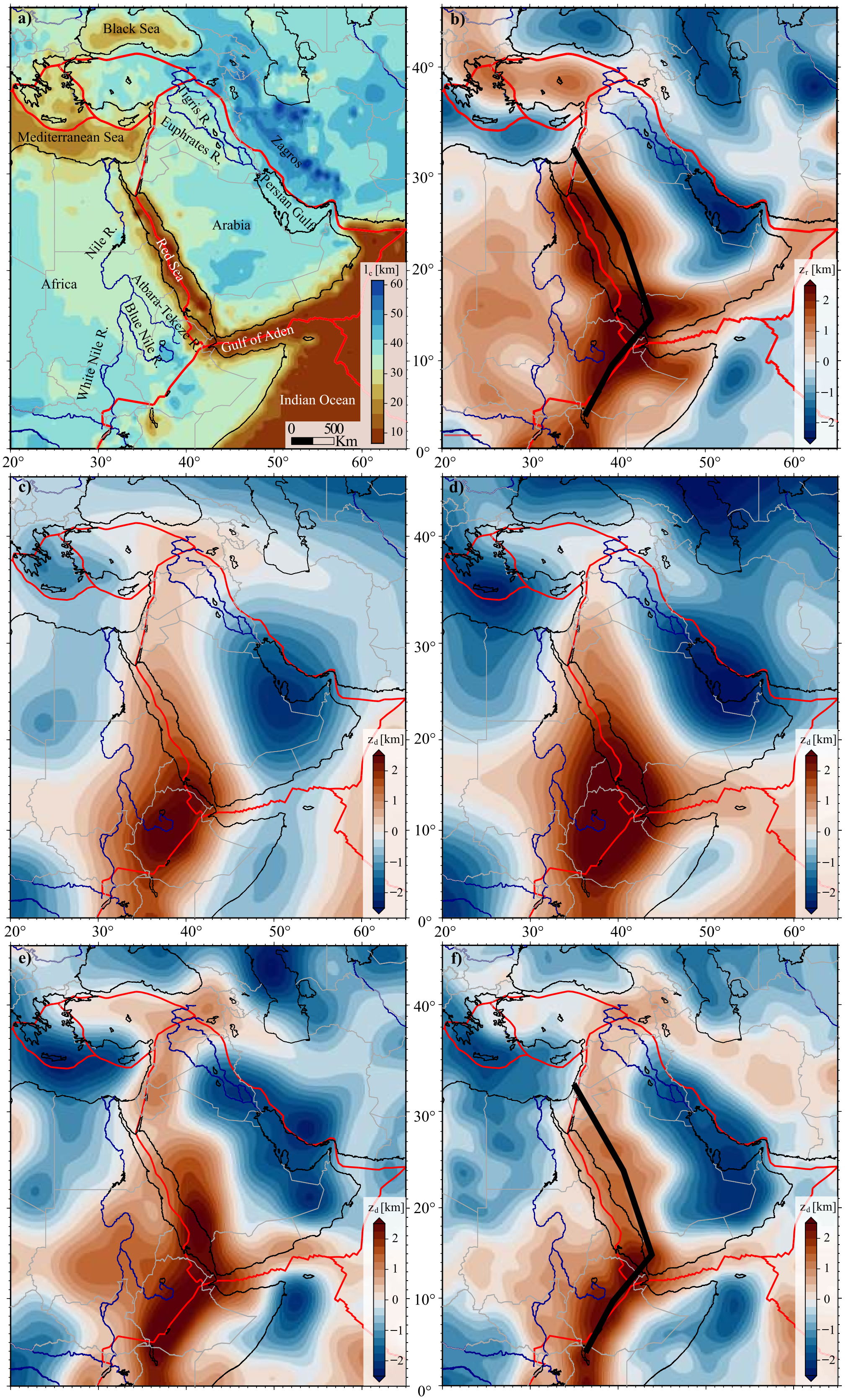

Fig. 10. a) Moho map based on a merger of CRUST1 (Laske et al., 2013) with constraints from regional studies (e.g. compiled in Gvirtzman et al., 2016), as in Faccenna and Becker (2020), but updated to also include the database of Boyce et al. (2023). b) residual topography based on crustal thickness and density variations, computed as in Faccenna and Becker (2020), but using a smoothed version of the new Moho map in a); c-e) dynamic topography based on mantle flow driven by scaling anomalies from TX2019 (c), SAVANI (d), SL2013 (e), and REVEAL (f, cf. Fig. 5), i.e. the seismic tomography models shown in Fig. 2. Residual and dynamic

topography computations follow Becker et al. (2014) and Faccenna and Becker (2020) but the wave speed anomaly to density scaling factors is reduced by 0.7 for models e) and f). The thick solid black line in b) and f) indicates the trace of profile represented in Fig. 13.

of the Zagros-Bitlis mountain belt (−1000–0 m), in the eastern sector of the Mediterranean Sea comprising the Nile River delta area (−1500–0 m), and in the western portion of the Indian Ocean (−1500–0 m), where we have not corrected for the effects of seafloor age dependent half-space cooling.

We can compare this lithospheric based estimate of anomalous residual topography with what deflections of the surface might be caused by mantle flow. At long wavelengths which allow ignoring flexural effects, those two anomalous topography estimates should match, assuming perfect knowledge of structure, density anomalies, and transport properties (see, e.g., discussion in Becker et al., 2014). We compute dynamic topography from a simplified, global mantle flow model with only radial viscosity variations by converting radial stresses to equivalent topography (e.g., Panasyuk and Hager, 2000), following the approach of Becker et al. (2014). On long wavelengths, this is a good approximation to the effects of mantle flow since dynamic topography of the surface is primarily sensitive to density anomalies in the uppermost mantle (e.g., Panasyuk and Hager, 2000), with only minor modifications due to lateral viscosity variations (e.g. Becker et al., 2014). Density anomalies are inferred by scaling seismic tomography with a constant scaling factor for all depths below 100 km, following Faccenna and Becker (2020), for simplicity. The seismic tomography models we use are, as in Fig. 2, TX2019 by Lu et al. (2019) (Fig. 10c), SAVANI by Auer et al. (2014) (Fig. 10d), SL2013 by Schaeffer and Lebedev (2013) (Fig. 10e), and REVEAL by Thrastarson et al. (2024) (Fig. 10f). Shear wave anomalies of models SL2013 and REVEAL have higher RMS than TX2019 or SAVANI and were scaled down by a factor of 0.7 to make overall anomalies comparable, sidestepping the general, unresolved issues of uncertain mineral physics scaling and uneven and model-dependent seismological anomaly recovery.

We therefore focus more on pattern than amplitudes, and the dynamic topography predictions based on the more recent, higher resolution models (Figs. 10e, f) indicate similar patterns to the residual topography one, implying that there is indeed a significant contribution from mantle processes to the non-isostatic, anomalous parts of topography. Moreover, comparison of the averaged shear wave velocity structure of Fig. 5 with the actual dynamic topography from flow prediction of the same model (Fig. 10f) highlights the aforementioned upper mantle density anomaly control of dynamic topography.

Positive values are concentrated along a roughly S—N trending strip from Ethiopia to Anatolia. The largest dynamic topography anomalies are found in part of Ethiopia, Eritrea, Djibouti, and Yemen. Positive anomalies up to 2000 m cover most of Sudan, the Red Sea, the western portion of the Arabian Peninsula, and the Middle East, up to Anatolia (Figs. 10c, d, e, f). Negative anomalies characterize the Somalian coast of Indian Ocean, northern Africa, eastern Mediterranean, and the Mesopotamian Basin-Persian Gulf area. This updated analysis broadly confirms earlier inferences (e.g. Daradich et al., 2003; Moucha and Forte, 2011; Chen et al., 2015; Faccenna and Becker, 2020), but Fig. 10 indicates an encouraging, improved regional match of residual and dynamic topography patterns.

The region represented in Fig. 10 is drained by two main drainage system: the Nile and the Euphrates-Tigris ones. The Nile River network is characterized by three main trunks: the White Nile, the Blue Nile, and the Atbara-Tekeze. While the first joined the main river network only in the Late Pleistocene (Williams, 2019), the Blue Nile and the Atbara-Tekeze rivers have a long history started at least in the Oligocene (Pik et al., 2003; Sembroni et al., 2016a; Faccenna et al., 2019; Sembroni et al., 2021). Indeed, geological and geophysical data (Garzanti et al., 2006; Padoan et al., 2011; Sembroni et al., 2016a; Faccenna et al., 2019) suggest that the deep mantle processes related to the upwelling of the Afar superplume created a stable topographic gradient which made the Blue Nile and the Atbara-Tekeze rivers stably connected to the Nile since at least 30 Ma.

Similarly, data from fluvial terraces (Demir et al., 2007; Stow et al., 2020) constrain the first appearance of the Euphrates River at the middle Miocene when the river flowed into the sea in southern Turkey. Successively, due to the regional uplift, the coast has shifted successively to the southeast resulting in the current path of the river (Demir et al., 2007; Stow et al., 2020). Demir et al. (2008), considering ~270 m of incision since the early Late Miocene (~9 Ma), estimated ~600 m of surface uplift on this timescale.

Plotting the drainage network on Fig. 10 we note that the Blue Nile-Atbara and the Euphrates-Tigris river networks source from areas of high positive residual and dynamic topographies (respectively the Ethiopian and the Eastern Anatolian plateaux) and end in regions of very low negative values (respectively the eastern Mediterranean Sea and the Persian Gulf).

Moreover, the area occupied by the swell (see Figs. 7 and 8) is characterized by the lowest values of lithosphere thickness in the region (Gvirtzman et al., 2016; cf. Fig. 2) and the highest residual and dynamic topographies (Fig. 10). P- (Benoit et al., 2006a; Hansen et al., 2012; Wei et al., 2019; Boyce et al., 2021, 2023) and S-wave (Benoit et al., 2006b; Priestley et al., 2008; Chang and Van der Lee, 2011; Schaeffer and Lebedev, 2013; Auer et al., 2014; Chen et al., 2015; Lu et al., 2019; Thrastarson et al., 2024) tomography indicates a low velocity anomaly at depths between 110 km and 300 km (Fig. 2). Moreover, the estimation of gravity effect of sediments all over the area results in a negative gravity anomaly region coinciding with the swell (Chen et al., 2015).

5.5. The geometry of the swell top surface

Previous studies demonstrated that during the Oligocene, several portions of the study area were characterized by low-relief surfaces which at present cover an area comprised of Ethiopia and the Levant (Coltorti et al., 2007; Gani et al., 2007; Avni et al., 2012; Bar et al., 2016; Sembroni et al., 2016a, 2016b; Sembroni and Molin, 2018; Sembroni et al., 2021). These surfaces are different in origin: the Levant and western Arabia ones are part of a wide planation surface separating the late Eocene – early Oligocene sediments from the late Oligocene - Holocene deposits (Avni et al., 2012; Bar et al., 2016) while the eastern Africa surface represents the top of the Oligocene basaltic plateau emplaced during or immediately after the impingement of the Afar superplume (Sembroni et al., 2021; Ebinger et al., 2024). At present, the surfaces stand at an elevation between 800 m (northern portion of the study area) and 2700 m (southern part).

To reconstruct the envelope of these surfaces, we mapped all the surfaces remnants by a spatial query in an ArcGIS environment (Fig. S1a). All surfaces with a slope lower than 3° and standing at an elevation ranging between 800 and 1200 m in the Arabian Peninsula and between 1000 and 2700 m in the Horn of Africa have been isolated (Fig. S1a). The surfaces have been then interpolated as a triangulated irregular network (TIN; Fig. S1b) and then smoothed by a circular low pass filter 100 km in radius to remove the artifacts related to the triangulation algorithm.

The result shows a surface whose trend changes from NE-SW in the southern portion to NNW-SSE in the northern one (Fig. 11). The elevation gradually decreases from south (2500 m) to north (900 m) for a total distance of ~4000 km from Ethiopia to Jordan. In Fig. 12 some images taken from Google Earth show examples of portions of the surface. This feature occupies the same region characterized by negative gravity anomaly (Chen et al., 2015), by P- and S-wave low velocity anomaly (Kendall et al., 2005; Benoit et al., 2006a, 2006b; Priestley et al., 2008; Bastow et al., 2010; Chang and Van der Lee, 2011; Hansen

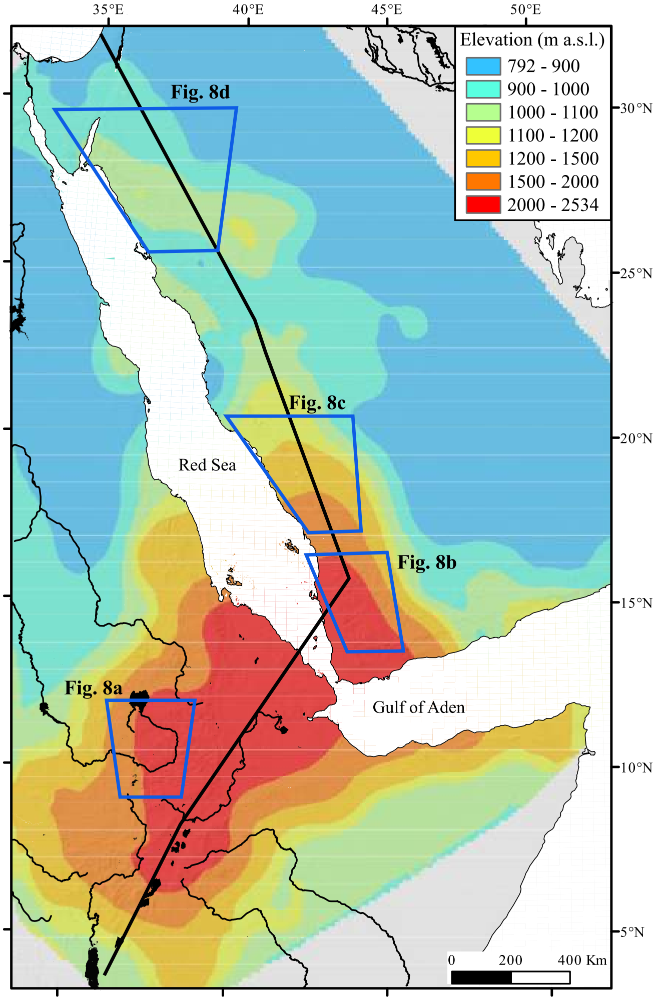

Fig. 11. a) The top surface of the East African-Arabia swell obtained by interpolating the isochronous high-standing surfaces mapped between Ethiopia and Jordan. The thick solid black line indicates the trace of the profile represented in Fig. 13.

et al., 2012; Schaeffer and Lebedev, 2013; Auer et al., 2014; Chen et al., 2015; Lu et al., 2019; Reiss et al., 2019; Wei et al., 2019; Chang et al., 2020; Hosseini et al., 2020; Andriampenomanana et al., 2021; Boyce et al., 2021, 2023; Saeidi et al., 2023; Ebinger et al., 2024; Thrastarson et al., 2024; Fig. 2), and by high residual and dynamic topographies (Fig. 10).

Lastly, to compare the geometry of the swell top surface with the trend of the filtered, residual, and dynamic topographies a profile for each has been extracted by using the same trace represented in Figs. 7b, 10b, f, and 11 (Fig. 13). The swell top surface profile matches quite well the residual and dynamic topographies. The same decreasing trend, even if with lower values, characterizes filtered topography at 400 km where the minimum at ~1250 km coincides with the Gulf of Aden-Red Sea rift system whose signal cannot be detected in the swell top surface. In summary, all the considered topographies show a decreasing trend from south to north with maximum values concentrated in the area comprising Ethiopia, Eritrea, Djibouti, and Yemen (Fig. 13).

5.6. *The distribution and age of volcanic deposits*

Since the Eocene, the study area was affected by widespread volcanism. To investigate the distribution and a possible age pattern of volcanic deposits, a compilation of 1465 volcanic samples has been analyzed expanding the databases previously published (Camp and Roobol, 1992; Bosworth and Stockli, 2016; Civiero et al., 2022; Hua et al., 2023; Fig. 14; see supplementary material for references – Table S2). Each sample is classified according to the country where it was sampled and the database has been cleared of all those deposits whose geochemical analyses showed a clear derivation from subduction processes (the “orogenic” deposits of Lustrino and Wilson, 2007). The study area has been divided into two parts: the southern portion (Ethiopia, Djibouti, Yemen, Saudi Arabia; Fig. 15a) and the northern one (Egypt, Israel, Jordan, Syria, Turkey; Fig. 15b).

The age frequency plots for both areas show a roughly bimodal distribution in accordance with previous studies (Camp and Roobol, 1992; Bosworth and Stockli, 2016; Civiero et al., 2022; Figs. 15a, b). In particular, the southern area presents the age ranges of 18–42 Ma and 0–16 Ma with peaks comprised between 28 and 32 Ma and 0 and 4 Ma respectively (Fig. 15a). These two ranges are separated by a brief period (16–17 Ma) of low volcanic activity well documented all over Saudi Arabia (Camp and Roobol, 1992; Bosworth and Stockli, 2016). In general, Ethiopia and Saudi Arabia are characterized by a quasi-continuous volcanic activity, while the ages of volcanic deposits in Yemen and Djibouti are comprised only between 32 and 20 Ma and 0 and 4 Ma, respectively (Fig. 15a).

In the northern area the bimodal distribution is shifted toward younger ages (Fig. 15b). In detail, the first range falls between 10 and 22 Ma while the second one is comprised between 0 and 8 Ma, with a remaining small number of samples with older ages (Fig. 15b). In contrast to the southern area, here the two ranges are separated by a sharp decrease in number of samples with ages comprised between 8 and 10 Ma. In general, except for Egypt, whose volcanic deposits ages vary between 18 and 32 Ma, in the remaining countries the volcanism is overall continuous (Fig. 15b).

The presence of young volcanic deposits in both areas may be in part because such deposits, outcropping at or near the surface, could cover the older ones. To investigate a possible pattern of volcanics age from the southern to the northern portions, the age data have been plotted against latitude following the example of previous studies (e.g., Bosworth et al., 2005; Bosworth and Stockli, 2016; Boone et al., 2021; Civiero et al., 2022). The result indicates a decrease in the maximum age of volcanic deposits from Ethiopia to Turkey with a plateau in coincidence with the Saudi Arabia data (Fig. 15c). By plotting on the same graph, the curve of filtered topography at 400 km extracted along the axis of the EAAS (Figs. 7b), it is possible to see a similar trend (excluding the Red Sea minimum) with elevation decreasing from ~1700 m in Ethiopia to less than zero in Jordan.

6. Discussion

The EAA swell covers the region from Ethiopia to Jordan crossing the Gulf of Aden and the Red Sea. Its configuration consists of a NNW-SSE trending ridge with amplitude and height decreasing from south to north. Most of volcanoes and basaltic lava fields are located along its axis. In general, the ridge appears asymmetric with respect to the Red Sea. This is possibly related to crustal thickening due to magmatic underplating as indicated by recent geophysical analysis in the central portion of the Arabian margin of the Red Sea which evidenced the presence of a magmatic body in the lower crust atop an underplated Moho (Mukhopadhyay et al., 2023). That portion is characterized at the surface by large volcanoes and basaltic lava fields dated between Tertiary and Quaternary (Coleman et al., 1983; Camp and Roobol, 1992). This configuration appears similar to the Main Ethiopian Rift one where the rift opened immediately to the east of the Ethiopian Plateau affected by a strong underplating during the Trap phase (Rooney, 2017), as evidenced by seismic refraction and receiver function data (Mackenzie et al., 2005; Tiberi et al., 2005).

The continuity of the swell is interrupted to the north in coincidence with the Mesopotamian Basin, considered as the foreland basin of the Bitlis-Zagros mountain belt. Here, a wide depression extending from

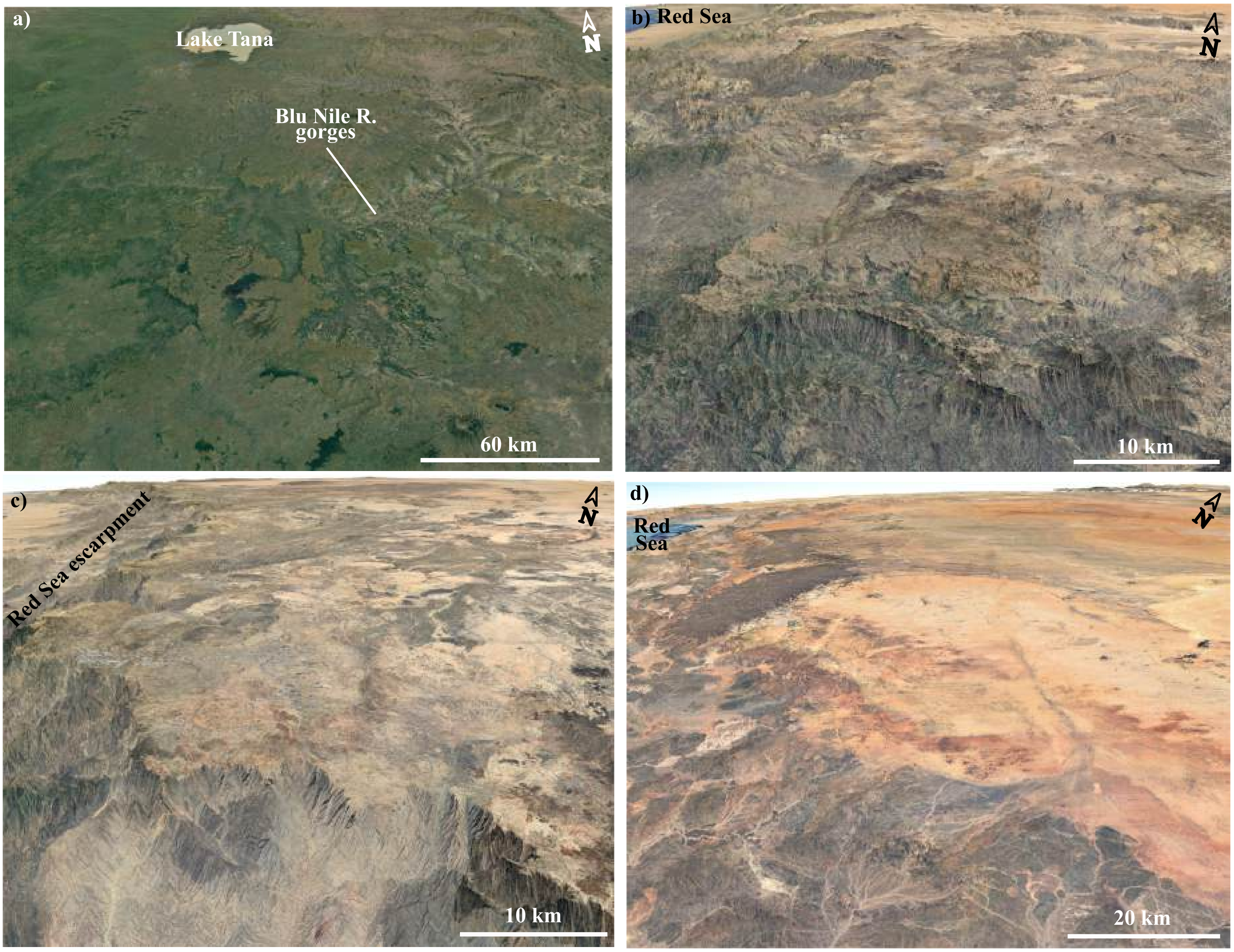

Fig. 12. Images from Google Earth showing portions of the Oligocene surface from Ethiopia (a), Yemen (b), western Saudi Arabia (c), and northern Saudi Arabia (d). Note the low-relief top surfaces in all figures which represent portions of the swell top surface. See Fig. 11 for the exact location.

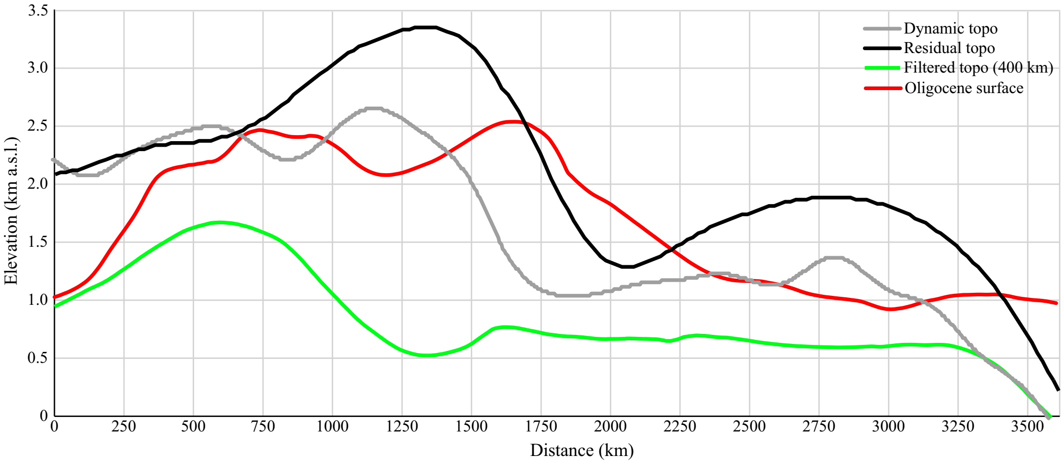

Fig. 13. Plot showing the trends of dynamic, residual, and filtered topographies (400 km) with respect to the Oligocene swell top surface along the solid black line drawn in Figs. 7b, 10b, f, and 11.

Syria to the Persian Gulf may be related to the depression of the lithosphere by subduction of the basement of the Arabian plate under the sedimentary rocks of the same plate (e.g., Yeats, 2012). This seems confirmed by the maps of dynamic topography (Figs. 10c, d, e,f) which, in accordance with previous studies (Gvirtzman et al., 2016; Steinberger, 2016; Faccenna et al., 2019; Steinberger et al., 2019; Lu et al.,

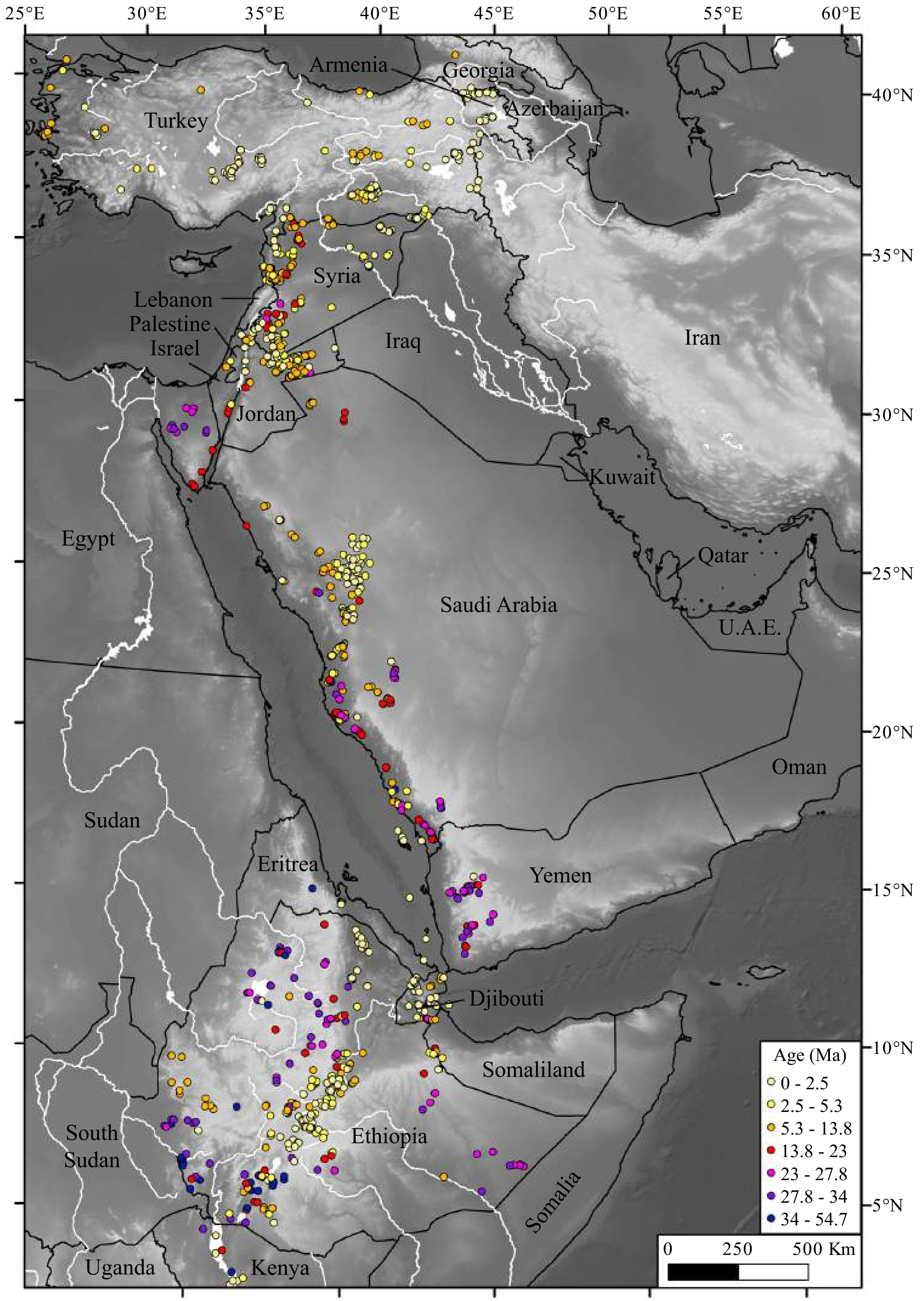

Fig. 14. Distribution of volcanic deposits along the study area distinguished by age.

2019), indicates negative values in the area. To the northwest, the swell is bounded by the easternmost portion of the Mediterranean basin characterized by negative values in filtered topography (Figs. 7a, b). As for the case of the Mesopotamian Basin, this area presents negative dynamic topography (Figs. 10c, d, e,f) related to the depression of the lithosphere induced by slab sinkers (Forte et al., 2010; Gvirtzman et al., 2016; Steinberger, 2016; Faccenna et al., 2019; Steinberger et al., 2019; Lu et al., 2019).

The incision (local relief) is low both on the top and on the flanks of the swell with the exception of the areas close to the Red Sea and Main

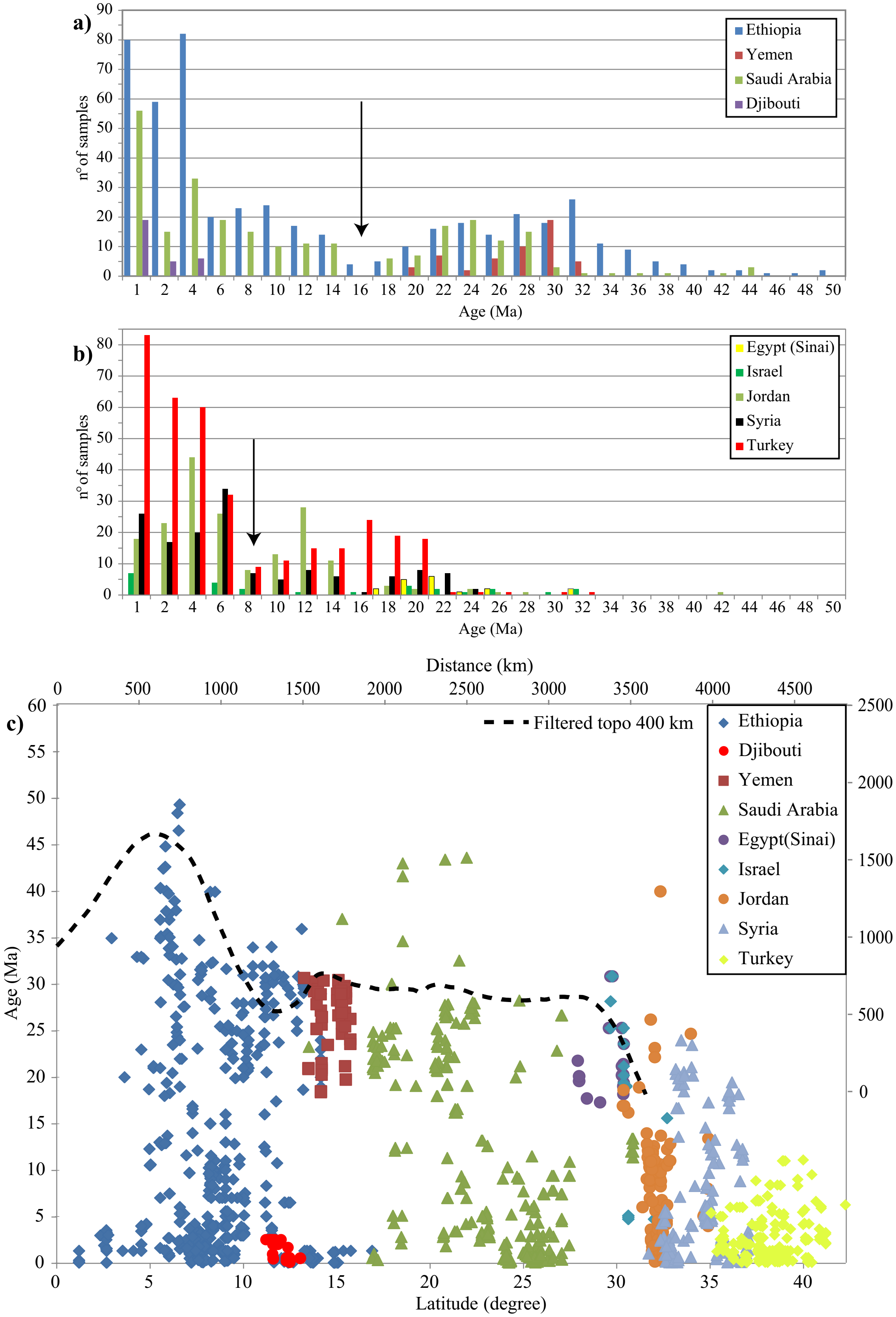

Fig. 15. a-b) Frequency plots of the volcanic deposits outcropping along the study area according to their ages; both plots show a bimodal distribution characterized by a marked minimum at 16–17 Ma in Fig. 15a and at 8–9 Ma in Fig. 15b; c) Distribution of the ages of the volcanic deposits according to latitude. Superimposed on the graph, the curve of the filtered topography at 400 km (the trace is shown in Fig. 7b) has been represented for comparison.